Satellite and Lidar Observations of the Albedo, Emittance and Optical Depth of Cirrus Compared to Model Calculations

C. M. R. PLATT

CSIRO Division of Atmospheric Physics, Aspendale, Victoria, Australia, 3195

DAVID W. REYNOLDS

Department of Atmospheric Sciences, Colorado State University, Fort Collins 80523

N. L. ABSHIRE

Wave Propagation Laboratory, NOAA, Boulder, CO 80302

(Manuscript received 14 August 1979, in final form 21 November 1979)

ABSTRACT

Radiometric data from the SMS-2 and GOES-1 geostationary satellites together with ground-based lidar scans have been combined to determine the visible albedo, infrared emittance and visible optical depth of cirrus clouds. The combined observations were made on an area of cirrus of about 10 km by 10 km square at Boulder, Colorado during two days.

A method of analysis was developed to separate out the cloud albedo from surface albedo effects, to allow for possible anisotropy in the bi-directional reflectance of solar radiation from the clouds, and to compare the data with results of theoretical calculations.

Relations between the visible albedo and the infrared emittance, which were derived from satellite data, and the visible optical depth, which was derived from lidar measurements, were compared with theoretical relations derived from two models of cloud particle scattering. The first model assumes that the cloud is composed of water (or ice) spheres and the second that it is composed of long ice cylinders. It was found that the observational data agree best with the latter model, although there are still some discrepancies.

The infrared emittances varied between 0.2 and 0.95, the corresponding albedos between 0.10 and 0.32 and the visible optical depths between 0.5 and 3.5.

1. Introduction

This paper describes an attempt to deduce the visible (solar) albedo of cirrus from geostationary satellite radiance measurements and to compare the albedo so obtained with that computed theoretically for various cloud models.

The visible albedo is an important cloud parameter as it determines the amount of solar radiation reflected back to space. The scattering phase function, and therefore the albedo, of water clouds can be calculated from Mie theory for any given cloud drop-size distribution and depth (e.g., Hansen, 1969). There is yet no equivalent theory for scattering from ice crystals in cirrus clouds, although scattering by hexagonal ice crystals has been computed by ray-tracing methods (Jacobowitz, 1971). Some progress has been made toward an analytical solution by assuming that the scattering properties of bulk ice crystals in a cloud can be approximated by long ice cylinders of appropriate dimensions (Liou, 1973). The two main ice crystal habits to be found in high cirrus clouds are columnar and long hexagonal crystals which are both approximately cylindrical in shape. Comparison of the few laboratory measurements of the scattering patterns of ice crystals together with Jacobowitz's calculations indicates that a model of cylinders gives a better representation of ice crystal scattering than does a model of spheres (Liou, 1973). Now the visible albedo of an extended cloud calculated from a model of ice cylinders is ~60% higher (but varying somewhat with solar angle and visible optical depth) than the equivalent albedo for a model of water (or ice) spheres (see Fig. 1). This is an appreciable difference and from the point of view of prediction of the climatic and dynamic effects of cirrus clouds (e.g., Stephens and Webster, 1979) it is important to determine whether either of the above theoretical cloud models gives sufficiently realistic results.

In this article the albedo which is deduced from satellite visible radiometric observations is plotted

0027-0644/80/020195-10$06.50

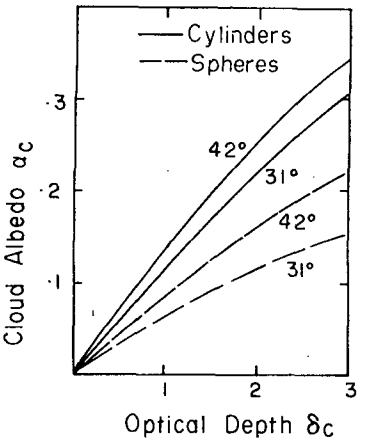

FIG. 1. Relations between albedo α_c and optical depth δ_c for two models of a cloud. The angles give solar zenith angle. The curves were taken from the results of Hansen (1969) for water spheres and Liou (1973) for ice cylinders.

against the infrared (IR) emittance[1] (10–12 μm) derived from satellite radiometric observations and also against the visible optical depth derived from ground-based lidar data. These plots are then compared with appropriate theoretical curves using both the cylinder and sphere scattering models. The theoretical albedos were taken from the work of Liou (1973) for cylinders and from Hansen (1969) for spheres. The relations between the visible and IR optical depths are also taken from appropriate theoretical results (G. L. Stephens, private communication).

The theory of the optical quantities is given in Section 2. The lidar and satellite observations are described in Section 3 and the analysis of the data is given in Section 4. Methods of averaging and comparing the satellite and lidar scans are described in Section 5. A discussion of how the cloud albedo is calculated from the total observed albedo is given in Section 6 followed in Sections 7 and 8 by comparison and discussion of the various observed optical quantities.

2. Relations between cloud optical quantities

The quantities which are compared in this article are the cloud albedo α_c, the cloud optical depth δ_c and the cloud IR emittance ϵ.

For a given particle distribution and type, the cloud albedo α_c is a function of the (vertical) optical depth δ_c and the solar angle of incidence θ. Examples of the results of computations of albedo α_c for an infinite, homogeneous cloud composed of either water (or ice) spheres (taken from Hansen, 1969) or long ice cylinders (taken from Liou, 1973), and for two solar angles, are shown in Fig. 1.

[1] The term emittance replaces the previously used emissivity in compliance with new radiation terminology.

In order to compare α_c against IR emittance ϵ it is necessary to have a theoretical relation between the cloud visible optical depth δ_c and the emittance ϵ. The assumption is made that

$$\delta_a/\delta_c = g, \tag{1}$$

where δ_a is the absorption optical depth at 10–12 μm and g is the same for all cirrus clouds. This is a reasonable assumption if the cloud particles are large compared to the wavelengths, which is generally the case for cirrus (Platt, 1979).

Then, if scattering effects are neglected,

$$\epsilon = [1 - \exp(-g\delta_c)]. \tag{2}$$

It is thus possible to obtain a relation between the cloud albedo α_c and the cloud (vertical) emittance ϵ for any given solar angle and cloud model.

The cloud optical depth can be calculated from the lidar integrated backscatter $\gamma(\pi)$ using the formulas (Platt, 1979)

$$\delta_c = \frac{\gamma(\pi)}{k}, \tag{3}$$

$$\gamma(\pi) = \int_{z_0}^{z_T} B(\pi,z)dz, \tag{4}$$

where z_T is cloud top, z_0 cloud base, $B(\pi,z)$ the isotropic backscatter coefficient and k the backscatter-to-extinction ratio.

The quantity measured by the lidar is the attenuated backscatter coefficient $B'(\pi,z)$. This can be corrected for cloud attenuation using the formula (Platt, 1979)

$$B(\pi,z) = B'(\pi,z)\left[1 - (2/k_e)\int_{z_0}^{z} B'(\pi,z'')dz''\right]^{-1}, \tag{5}$$

where k_e is an effective backscatter to extinction ratio and $k_e = k/\eta$, where η is a multiple-scattering factor.

The value of k_e is given experimentally by a series of lidar measurements when the cloud becomes optically thick. It can be shown that attenuated integrated backscatter

$$\gamma'(\pi) = \int_{z_0}^{z_T} B'(\pi,z)dz,$$

tends to the value of $k_e/2$ as δ_c becomes large (Platt, 1973). A value of η can be obtained from past measurements (Platt, 1973).

3. Lidar and satellite observations

Lidar observations of the cirrus clouds were made with the WPL/ERL/NOAA lidar (Derr *et al.*, 1976) at Table Mountain about 13 km north of Boulder. The observations were timed to coincide with scans of the same clouds by the VISSR (Visible and Infrared Spin Scan Radiometer) instruments of

the SMS-2 and GOES-1 geostationary satellites (hereafter called GOES-W and GOES-E, respectively).

The lidar was scanned from the vertical out to a zenith angle of 50° for four different azimuths, varying from 16 to 106°, and thus covering one quadrant of the sky. The scan area was away from the Rocky Mountains which rose a few kilometers to the west. The area of cloud which was scanned was approximately 10 km by 10 km at an altitude of 8 km. A total scan took about 2 min to complete.

The geostationary satellites scan the earth in an asymchronous fashion, i.e., GOES-E takes data on the hour and half-hour while GOES-W takes data 15 min after and 15 min before the hour. Sections of satellite data were recorded at full spatial resolution with nominal spot sizes at Colorado of 1.0 km north-south by 1.0 km east-west for the visible sensor and 8 km north-south by 4 km east-west for the infrared sensor.

Data were recorded over parts of Wyoming and Colorado, as shown in Figs. 2 and 3. Data for this study were then selected from a target area, a rectangular area 18 km by 22 km with the southwestern corner located over the lidar site, and thus encompassing the lidar scan area.

The data were navigated into earth coordinates to an accuracy of 1–2 km by using known landmarks in the vicinity of the target area. Because each picture was registered with respect to the others, one line-element to latitude-longitude transform taken at one time sufficed for all other times, including those when the target area was covered by cloud.

4. Analysis of data

The NOAA lidar was calibrated, so that received voltages could be converted to units of isotropic attenuated backscatter coefficient $B'(\pi)[\mathrm{m}^{-1}]$. The Rayleigh and aerosol backscatter contributions were subtracted from the lidar profiles. The values of $B'(\pi)$ were then corrected for pulse attenuation in the cloud using Eq. (5). They were also corrected for a known linear change in lidar gain with angle.

FIG. 2. Satellite image around the target area. Visible channel, GOES-W, 1915 GMT 16 March.

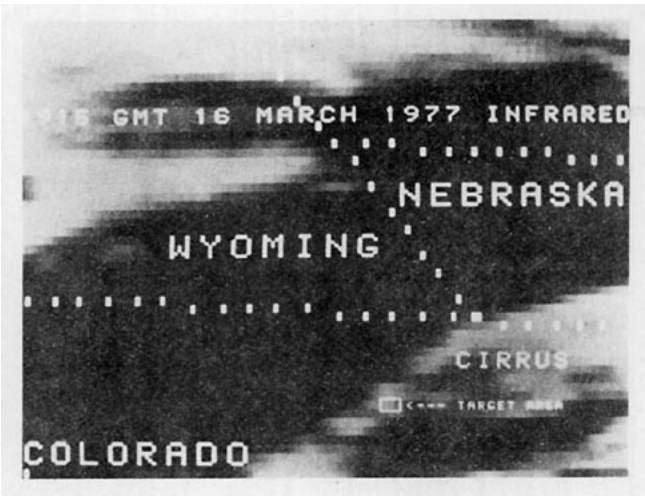

FIG. 3. As in Fig. 2 except for the IR channel.

From an examination of values of $\gamma'(\pi)$ at periods when the cloud optical thickness became large, $k_e/2$ was estimated as 0.2 ± 0.02.

Values of $\gamma(\pi)$ for each lidar shot were calculated by numerically integrating $B(\pi,z)$ at height intervals of 10 m in the cloud.

The optical depth δ_c was calculated using a value of η equal to 0.4 ± 0.1 (Platt, 1973) so that $k(=2\eta k_e) = 0.16 \pm 0.05$. The optical depth was then normalized to its vertical value by multiplying by the cosine of the lidar scan zenith angle.

Neither the GOES-E nor GOES-W satellite visible radiometers were calibrated and it was necessary to use the pre-launch calibrated radiometer on board the NOAA-2 polar orbiting satellite as a reference. This radiometer had the same spectral response characteristics as the SMS/GOES series of satellites. A transfer regression due to Smith and Loranger (1977)[2] between the raw SMS-1 visible count and the normalized instantaneous isotropic albedo as measured by the NOAA-2 satellite was adopted in the present study. The GOES-W flew practically the same instrument as used on SMS-1 and the estimated maximum error between the calibration of the two instruments was 5%. The GOES-E had a calibration uncertainty of 10% and the GOES-E radiometer counts were accordingly normalized to the GOES-W radiometer. This was done by comparing the counts recorded from three surface features; plains ($\alpha \approx 0.2$), tree-covered foothills ($\alpha \approx 0.1$) and the tops of thick synoptic-scale cloud systems ($\alpha \approx 0.6$). It was found that GOES-E consistently measured a lower albedo than GOES-W and the adjustment pro-

[2] Copies of this article are available from the Department of Atmospheric Sciences, Colorado State University.

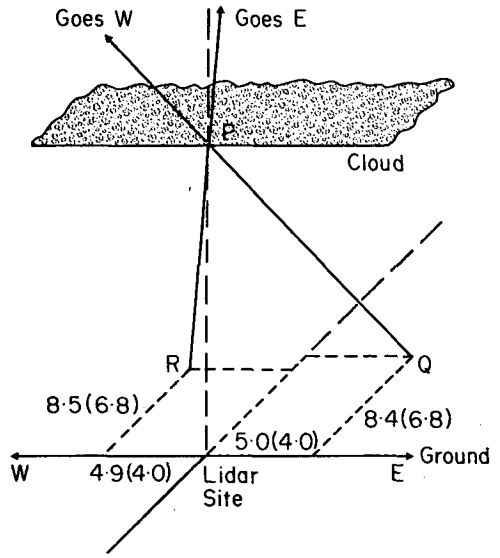

FIG. 4. Schematic showing projection of lidar sampled area of cloud away from navigated lidar site. Numbers show displacements (km) for 16 March and 14 April (in parentheses).

cedure was to add 5 counts to the GOES-E 8-bit visible measurements. This correction contributed an extra 1–2% to albedos of 30–35%.

The analysis of the IR data from the VISSR was more straightforward. IR digital counts were related to equivalent black-body temperatures through a standard table which is regularly updated by the Wallops Island ground station. Effects of atmospheric water vapor absorption in the 10–12 μm interval were considered to be negligible for the atmospheric path under consideration.

The IR temperatures were converted to radiances using the Planck function integrated over the satellite radiometer filter factor. If $L(\zeta)$ is the measured radiance over a cloud, $L(G)$ the equivalent radiance from the ground at cloud-base level and $L(B)$ the blackbody radiance at cloud temperature, then, neglecting scattering, the emittance $\epsilon(\zeta)$ at a viewing zenith angle of ζ is given by (e.g., Shenk and Curran, 1973; Platt, 1975; Reynolds and Vonder Haar, 1977)

$$\epsilon(\zeta) = \frac{L(G) - L(\zeta)}{L(G) - L(B)} . \tag{6}$$

In the present study values of $L(B)$ corresponded to mid-cloud temperatures. Mid-cloud altitudes were obtained from the lidar data, and temperatures from the 1200 GMT Denver upper air sounding. The surface radiances $L(G)$ below the cloud were determined from the IR data from cloud-free areas near the target area. GOES-W surface IR radiances were used to calculate emittances.

For comparison of measured cloud albedos with emittance the vertical emittance ϵ_v was calculated.

The IR optical depth at a satellite zenith angle of ζ is given by

$$\delta_a(\zeta) = -\ln[1 - \epsilon(\zeta)] \tag{7}$$

and the vertical emittance ϵ_v is given by

$$\epsilon_v = 1 - \exp[-\delta_a(\zeta) \cos\zeta]. \tag{8}$$

5. Comparison of satellite and lidar scans

16 March 1977 was an excellent day for study in that conditions were perfectly clear except for cirrus clouds moving in from the southwest over the lidar site, ahead of an upper trough. Figs. 2 and 3 show the visible and infrared images from GOES-W for this day at 1915 GMT when the northern edge of the cirrus was directly over the site. Note that the infrared data tend to highlight the cirrus clouds better than the visible.

A problem occurs in the comparison of the lidar and satellite scans because the cirrus cloud is situated at altitudes varying from 6 to 9 km above the surface. Thus, when viewed from the satellite a point directly over the lidar site is, as illustrated in Fig. 4, projected on to the surface at either point Q or R depending on whether the satellite is GOES-W or GOES-E. For the conditions pertaining at Boulder, and for mean cloud heights of 7.6 km (16 March) and 6.1 km (14 April), the horizontal distances of points Q and R away from the lidar site are as shown. As the satellite data grids in the target area were navigated with surface coordinates, then the areas of data corresponding to the horizontal area of cloud scanned by the lidar are also shifted on the data grids.

Allowing for the above shifts, the values of albedo, IR radiance and IR temperature were averaged over the corresponding lidar scan areas. Values of integrated lidar backscatter $\gamma(\pi)$ were similarly averaged.

Fig. 5 is a time history of the average albedo α_m. The albedoes show considerable variations from one period to the next, but the main feature is the presence of large albedos between 1900 and 1930 GMT. There is a correspondingly lower average infrared brightness temperature, indicating denser clouds during this time. By 1945 the cirrus was clearing the site. Note that there is a systematic albedo difference between the two satellites, particularly when the cloud cover is thin and semi-transparent. This is due to the fact that the surface albedos which the two satellites partially see at Q and R (Fig. 4) are different.

At 1945, when the scan area was free of cirrus, the surface background albedo for the GOES-W satellite was 0.2. The ground albedo for the GOES-E satellite was much lower, with a value of 0.11. The projected field of view of this satellite through the cloud over the lidar site was the wooded foothills of the Rockies, while the GOES-W field of view was over the plains.

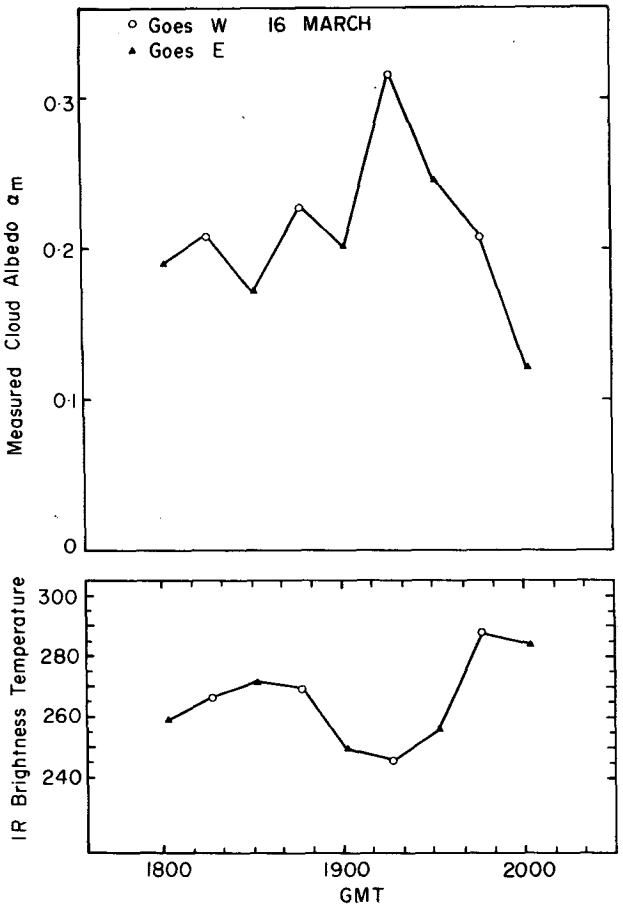

FIG. 5. Time history of averaged albedo α_m and IR brightness temperature for 16 March.

Figs. 6a and 6b illustrate contour maps of albedo and integrated lidar backscatter $\gamma(\pi)$, constructed from the (shifted) gridded albedo values in the former case and the spot lidar values along the four lidar scan directions in the latter. Although the albedo variations are not directly reproduced in the lidar scans, the general pattern is similar in the two cases.

Similar results were obtained on 14 April although only a limited amount of satellite data was available. Average albedos, emittances and mid-cloud temperatures are listed in Table 1.

6. Calculation of cloud albedo

The calculation of the cloud albedo from the measured albedo α_m must take several factors into account. First, atmospheric absorption and scattering above the cloud will modify α_m. However, the visible satellite radiometer detects between 0.51 and 0.89 μm wavelengths where there is only ~1–2% absorption of solar flux by ozone and an estimated 1% Rayleigh scattering. Furthermore, these two effects tend to cancel and are neglected here.

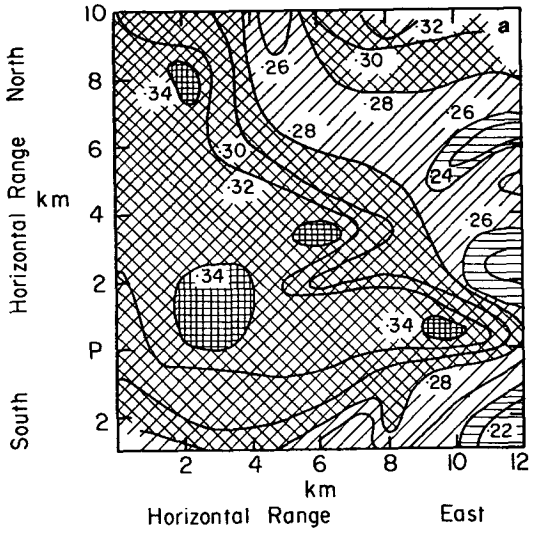

FIG. 6a. Contour plot of observed albedo in the projected lidar scan area for GOES-W, 1915 GMT 16 March.

The second factor is that the satellite measures a bidirectional reflectance and the reflectance of clouds, such as cirrus, which have a comparatively small optical depth, is by no means isotropic (e.g., Wendling, 1977). The GOES satellites generally observe solar radiation scattered in the back hemisphere, that is radiation scattered by more than 90°, and the satellite measures an apparent albedo $\phi(\zeta,\theta,\psi)\alpha$, where ζ and θ are zenith angles of the satellite and the sun, ψ is the azimuth angle between the solar and satellite planes, and α is the *isotropic* albedo.

The third factor is that the clouds are generally semi-transparent, so that both (attenuated) direct

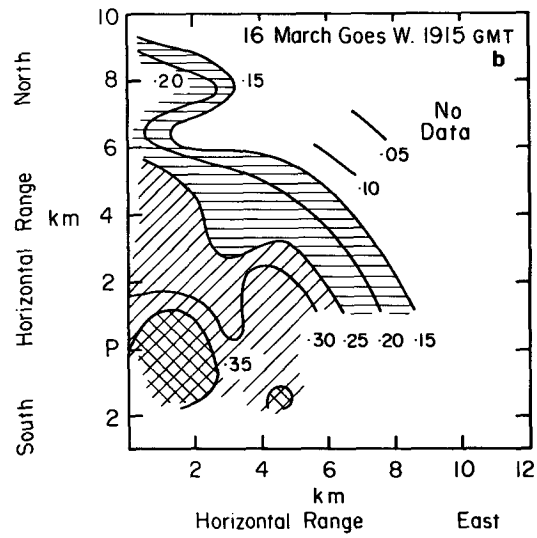

FIG. 6b. Contour plot of lidar integrated backscatter $\gamma(\pi)$. Lidar site is given as P.

TABLE 1. Observed and calculated cloud optical quantities.

Time (GMT)	θ (deg)	ζ (deg)	ψ (deg)	T^*	α_m	α_c	ϵ_v	$\gamma(\pi)$	δ_c
16 March									
1800	43	52	7	−48	0.19	0.10	0.40	0.078	0.50
1815	42	52	47	−47	0.21	0.045 (0.09)	0.36	0.085	0.53
1830	42	52	18	−47	0.17	0.09	0.31	0.114	0.71
1845	41	52	36	−46	0.23	0.095 (0.12)	0.36	0.081	0.51
1900	41	52	30	−46	0.20	0.11	0.61	0.167	1.05
1915	41	52	25	−42	0.32	0.24 (0.24)	0.65	0.283	1.72
1930	42	52	42	−41	0.25	0.17	0.55	0.221	1.38
14 April									
1845	31	52	37	−35	0.20	0.10	0.33	0.085	0.53
1915	31	52	24	−35	0.35	0.30	0.94	0.564	(3.53)
1945	32	52	10	−31.5	0.27	0.20	0.66	0.250	1.56

* Mid-cloud temperature.

and diffuse solar radiation which is reflected at the surface, is propagated back up through the cloud to the satellite.

The measured albedo α_m at the satellite is calibrated as explained in Section 4 assuming isotropy. The relation between α_m and the other cloud and surface parameters is

$$\pi^{-1}\alpha_m I_0 \cos\theta = \pi^{-1}\alpha_c I_0 \cos\theta\, \phi(\zeta,\theta,\psi) + \pi^{-1}\alpha_{g1} I_0 \cos\theta\, \tau_c^2 + \pi^{-1} I_0 \cos\theta\, \alpha_{g2}(1-\bar{\alpha}_c)(1-\tau_c-\alpha_c) \quad (9)$$

or

$$\alpha_m = \alpha_c\phi(\zeta,\theta,\psi) + \alpha_{g1}\tau_c^2 + \alpha_{g2}(1-\bar{\alpha}_c)(1-\tau_c-\alpha_c). \quad (10)$$

The first term on the right-hand side accounts for direct reflection from the cloud and the second and third terms account respectively for direct and diffuse radiation which is transmitted by the cloud and reflected at the surface.

In these equations, α_{g1} is the surface reflectance in the projected satellite line of sight, (i.e., at points R and Q in Fig. 4), α_{g2} the effective surface reflectance to diffuse radiation over a suitable area directly below the cloud, α_c the cloud albedo at zenith angle θ, $\bar{\alpha}_c$ the albedo of the cloud to diffuse radiation and τ_c the cloud transmittance to direct radiation (for $\theta \approx \zeta$).

In order to solve Eq. (10) for cloud albedo α_c in terms of α_m, it is necessary to know, among other quantities, the cloud transmittance τ_c. This quantity is not known implicitly and it can only be inferred through theoretical relations between the cloud albedo α_c and the optical depth δ_c, such as those shown in Fig. 1, and by the equation $\tau_c = \exp(-\delta_c)$. However, we are trying to *infer* a relationship between α_c and δ_c (or ϵ_v) from the experimental data so that strictly Eq. (10) should be solved by an iterative method, where the relationship between α_c and δ_c was given by an analytical formula with adjustable parameters. In the present case, it was considered that the accuracy of the data did not warrant such a detailed analysis and the procedure was to solve for α_c using the α_c-δ_c relationships from the cylinder scattering model, to test the results for consistency with the model, and then to compare these with similar results using the α_c-δ_c relationships from the sphere model.

More detailed consideration of the transmittance of solar radiation through a cirrus cloud indicates that roughly half the radiation which is scattered is diffracted radiation which assumes a direction very close to the forward direction (e.g., Platt, 1973). Thus, the diffracted radiation can be considered from the point of view of Eq. (10) as unscattered (e.g., Fritz, 1954). The effective optical depth is then reduced to $\delta_c/2$ and $\tau_c = \exp(-\delta_c/2)$.

Another quantity which is required for solution of Eq. (10) is the diffuse albedo $\bar{\alpha}_c$. This is related to α_c through

$$\bar{\alpha}_c = \frac{\int_0^{\pi/2} \alpha_c(\theta)\cos\theta d(\cos\theta)}{\int_0^{\pi/2} \cos(\theta) d(\cos\theta)}. \quad (11)$$

The procedure used here was to write $\bar{\alpha}_c$ as $f(\theta)\alpha_c$, where $f(\theta)$ varied only with θ, and to use a single value of f for a mean θ for each day. In point of fact $f(\theta)$ depends on cloud optical depth δ_c as well as zenith angle θ, as shown in Table 2, but the errors in using a single value of $f(\theta)$ were small (see Appendix).

The other term in Eq. (10) which is not known to any degree of accuracy is the anisotropy factor $\phi(\zeta,\theta,\psi)$. Generally, ϕ is less than unity in the back direction, that is, when the bireflectance angle between the solar direction and the satellite direction is less than 90°; but there is a local maximum in radiance when the bireflectance angle becomes very

small, as when $\zeta \approx \theta$ and the azimuth ψ is zero (Wendling, 1977). Wendling has computed the cloud radiance for a solar zenith angle of 45° (in the back direction), for $\psi = 0$, for a water cloud, and for $\delta_c = 5.85$. An estimate from his results puts the value of $\phi(\zeta,\theta,\psi)$ close to unity for $\zeta \approx 52°$, the satellite zenith angle in the present work. In the present case the cirrus cloud was ice, the value of θ was somewhat less than 45° and ψ was variable (the bidirectional angle varied from 5° to 40° during the periods of observation), so that conditions were not equivalent. However, for want of better information Wendling's value of unity was used for $\phi(\delta,\theta,\phi)$ with an uncertainty estimated from Wendling's curves of ±10%.

FIG. 7 shows the calculated relations between α_m and α_c using Eq. (10). Values of $f(\theta)$, α_{g1} and α_{g2} used for the different satellites and periods are also shown. The full lines correspond to the use of the cylinder model to give the requisite relation between α_c and τ_c. The broken line corresponds to the use of the sphere model.

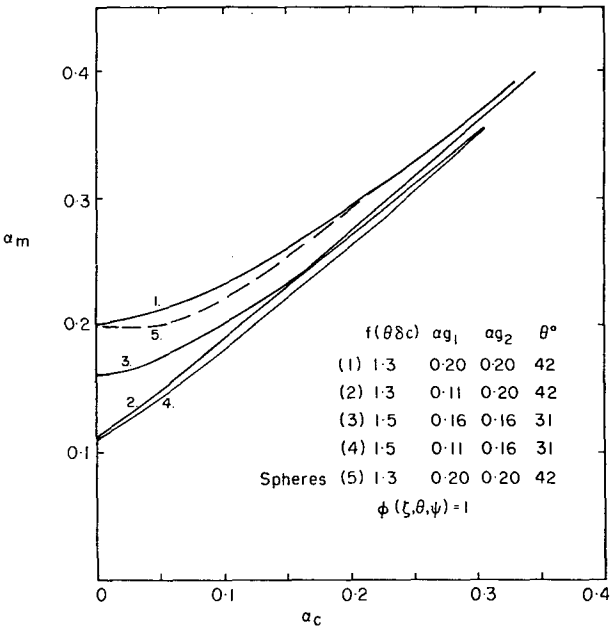

FIG. 7. Calculated albedo α_m vs cloud albedo α_c for the various conditions listed.

7. Results

Values of the angles θ, ζ, ψ, and calculated values of α_c and δ_c are shown in Table 1. Values of α_c were read off from the relevant curves of Fig. 7 for the corresponding values of α_m listed in Table 1.

Fig. 8 compares the variations with time of α_c and $\gamma(\pi)$ for 16 March. The IR brightness temperature is again shown for comparison. Despite some irregularities, which can be attributed to navigational errors together with differences in resolution between the various data sources, the broad changes in cloud properties with time are reproduced in both α_c and $\gamma(\pi)$. The systematic differences between the albedos α_m measured by the two satellites (Fig. 5) have now disappeared.

Fig. 9 shows values of α_c plotted against emittance ϵ_v. The theoretical curves for the two scattering models were calculated from Eq. (2) together with the curves of α_c versus δ_c shown in Fig. 1. The two values of g used were 0.50 for cylinders (G. L. Stephens, private communication) and 0.57 for spheres (Platt, 1973).

Values of α_c plotted against lidar-derived values of cloud optical depth δ_c are shown in Fig. 10. The albedo value for the densest part of the cloud (1915 GMT 14 April) is omitted. The error in the calculation of δ_c for an uncertainty in k_e of 30% is predicted to be large for this sort of value of α_c. However, the albedo value would lie roughly on the cylinder curve.

TABLE 2. Variation of diffuse cloud factor $f(\theta,\delta_c)$ with solar zenith angle.

δ_c	30°	40°	45°
1	1.9	1.5	1.4
2	1.4	1.2	1.1
3	1.3	1.15	1.1

8. Discussion

The observed dependences of cirrus albedo on IR emittance ϵ_v and visible optical depth δ_c are seen to be broadly in agreement with theoretical predictions. Furthermore there is better agreement with the cylinder model than with the sphere model, particularly in Fig. 10. However, it is recalled that values of τ_c used in Eq. (10) to calculate the relations between α_m and α_c were derived using the curves of α_c vs δ_c for the *cylinder* model. It is thus necessary to consider the magnitude of the change in the calculated values of α_c when using values of τ_c predicted from the sphere model. For this purpose we use curve 5 of Fig. 7 to derive values of α_c for the GOES-W data of 16 March. The values are shown bracketed in Table 1, and it is evident that they have *increased*, at least at the lower values. These, new values for α_c are thus not consistent with theoretical curves for spheres which actually give *lower* values for α_c compared to the cylinder model, so that the discrepancy between the data and the theory is increased.

In order to justify the apparent conclusion that the cylinder model gives a reasonable albedo prediction for cirrus clouds, it is necessary to estimate the magnitudes of the various error sources which are involved in the calculation of α_c, ϵ_v and δ_c. This

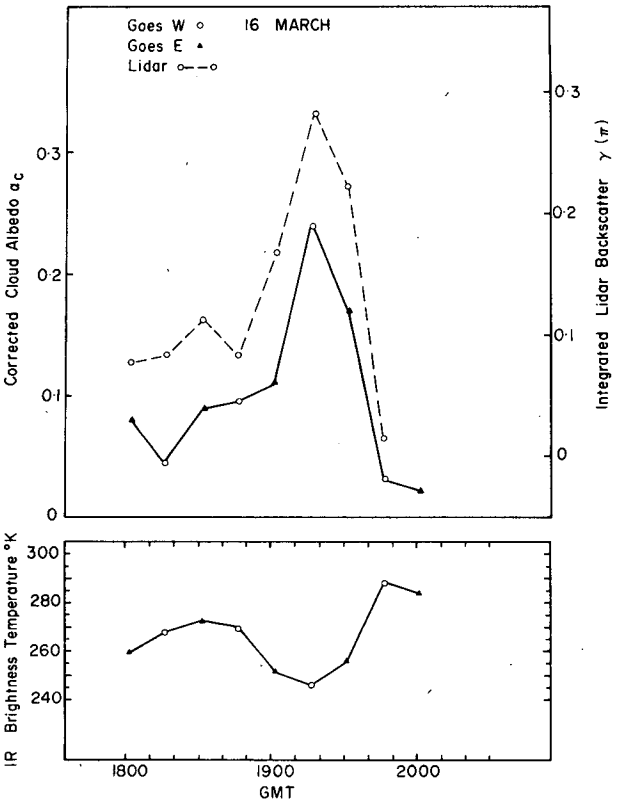

FIG. 8. Time histories of cloud albedo α_c, integrated lidar backscatter $\gamma(\pi)$ and IR brightness temperature for 16 March.

is also necessary to reconcile the somewhat different relations of the data points to the predicted curves in Figs. 9 and 10.

First we consider the data of Fig. 9. One error in the calculation of IR emittance from Eq. (6) is the neglect of cloud scattering effects. Scattering by cloud particles is forward-peaked about the original beam so that its effects are minimal. However, what effect there is reduces the radiance $L(\zeta)$ slightly, so that the calculated emittance is somewhat greater than the absorption emittance predicted from Eqs. (1) and (2). The magnitude of the change is not well known and is the subject of a current investigation; however, it is not likely to be more than about 10% of ϵ_v for midlatitude cases. A correction for this effect would decrease the values of ϵ_v, so that the agreement of the data with the predicted curves for cylinders would improve, which would in turn make the data more consistent with Fig. 10.

The various other error sources in the calculation of α_c are discussed in the Appendix. The largest systematic error lies in the assumption that $\phi(\zeta,\theta,\psi) = 1$. The estimated $\pm 10\%$ uncertainty in ϕ leads to a 5% (systematic) error in values of α_c. Other error sources discussed in the Appendix lead to an estimated additional uncertainty of $\pm 3\%$.

The error in α_c caused by the neglect of the effects of atmospheric absorption and scattering between the cloud and the satellite is conservatively estimated to be 2%.

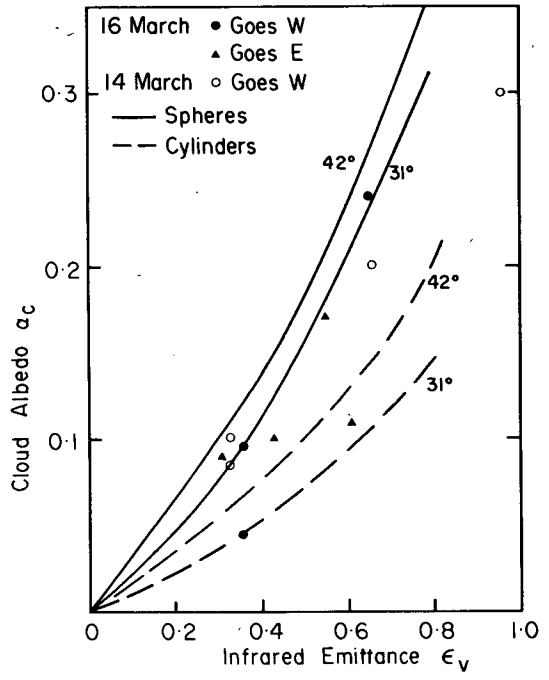

FIG. 9. Plot of cloud albedo α_c versus cloud vertical emittance ϵ_v. Also shown are predicted curves for the two model clouds (see text).

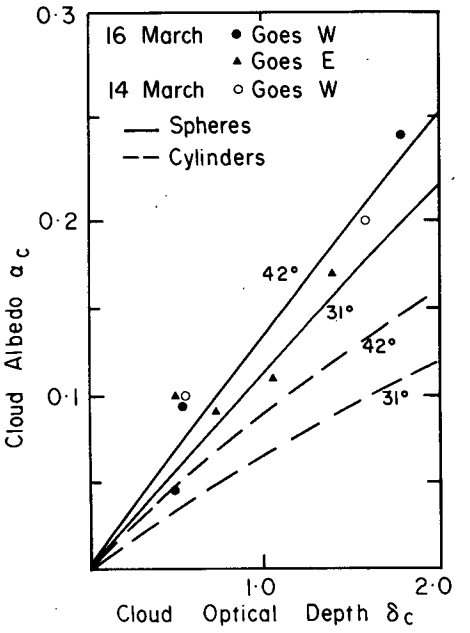

FIG. 10. Plot of cloud albedo α_c vs lidar-derived cloud optical depth δ_c. Predicted curves for the two model clouds are also shown (see text).

Added to the above errors is a 4–5% uncertainty in the satellite radiometer calibrations. However, as this error would appear in the values of α_{g1} and α_{g2} as well as α_m, the effects on deduced values of α_c would tend to cancel.

Total systematic uncertainty in the calculation of α_c is thus about ±7%. This is less than the observed random scatter in the data, and much less than the difference in α_c between the two models (~60%).

An additional error incurred in the values of δ_c is caused by the estimated ±30% (systematic) uncertainty in the value of k_e. This causes an error of ±25% in δ_c for $\delta_c = 0.5$ and a ±35% error in δ_c for $\delta_c = 1.5$ (Platt, 1979). However, even with this systematic error, the data still favor the cylinder model. It is perhaps significant that the scatter in the data due to random error is less in Fig. 10 than in Fig. 9. This points to a significant error in the calculation of ϵ_v which would be likely because of the poor resolution of the satellite IR data compared to the area of cloud investigated.

9. Conclusion

The observations on cirrus cloud described here represent a first attempt to extract high-cloud albedo data from satellite observations and to compare these with both simultaneous satellite IR 10–12 μm data and cloud visible optical depths measured with a ground-based lidar.

The method of analysis uses a more detailed procedure to separate the cloud reflection from transmitted surface diffuse and direct reflection than has been used hitherto. The analysis also allows for the anisotropy of the bireflectance of the cloud from the solar direction to the satellite; the need for accurate figures of the anisotropy factors under varying conditions is clearly demonstrated.

The equation [Eq. (10)] for the cloud albedo α_c requires an iterative method for its solution, where the variables are contained in the relation between α_c and the visible optical depth δ_c. This requires an analytical relation between α_c and δ_c with adjustable parameters. However the only theoretical relations available are those for the water (or ice) sphere cloud model and the cylinder model which are described in this article. As a result only the two models have been used to solve the α_c, the calculated values of α_c being tested in each case for consistency. The results have been shown to be more consistent with the cylinder model.

The differences in albedo predicted by the two scattering models, for given values of δ_c and solar angle θ, are very appreciable (see Fig. 1). Physically, these differences lie in the values of the asymmetry parameter $\langle s \rangle$ for the two cases. This parameter describes the fraction of the total radiation which is singly scattered in the back direction. For a cloud where $\delta_c \ll 1$, so that multiple scattering is negligible, $\alpha_c = \frac{1}{2}(1 - \langle s \rangle)$. Quoted values for a spherical drop water cloud and a cylinder ice cloud are 0.88 and 0.73, respectively (Hansen, 1969; Liou, 1973). These differences in $\langle s \rangle$, which can be traced to basic differences in the angular scattering phase function, thus explain the large equivalent differences in albedo.

The closer agreement of the observational data with the cylinder model is consistent with Liou's (1973) findings that the cylinder model gives a scattering phase function in reasonable agreement with experimental scattering phase functions for ice crystals.

Careful navigation of the satellite data has led to a satisfactory correlation between cirrus albedo and lidar-determined optical depth, as shown in Fig. 10. Figs. 6a and 6b also demonstrate that the general distribution of cloud, as given by the cloud albedo α_m, is reproduced in the contoured lidar maps. Fine-scale agreement within distances $\lesssim 2$ km would not be expected. The resolution of the albedo data is 1.2 km × 1.5 km, whereas the lidar took spot samples of cloud of ~50 m in diameter at 10 km range, and spaced at ~0.5–1 km apart.

The methods used in this article have general application to the determination of cirrus cloud amounts and optical properties. It is shown that a lidar can give information on cloud optical thickness. A lidar sounding continuously from space (e.g., Spacelab), *along with visible and IR radiometers*, would form a very useful system for the investigation of both cloud optical properties and for more accurate determinations of high cloud amounts.

Acknowledgments. The observational phase of this work was done while one author (C. M. R. Platt) held a Visiting Fellowship at the Cooperative Institute for Research in Environmental Sciences, Boulder, Colorado. The same author would like to thank Dr. V. E. Derr, Environmental Research Laboratories, NOAA, Boulder, for making the WPL/ERL lidar system available and for much encouragement; also Dr. G. T. McNice for assistance with the lidar measurements.

APPENDIX

Errors in the Correction of Measured Cloud Albedo α_m for Surface and Anisotropy Effects

The relationship between the actual cloud albedo α_c and the measured cloud value α_m is given by Eq. (10). Apart from neglect of scattering from other layers in the atmosphere (e.g., Rayleigh, aerosol), the parameters in which there is uncertainty are the surface albedos α_{g1} and α_{g2}, the functions $\phi(\zeta,\theta,\psi)$ and $f(\delta_c,\theta)$, and the relationship between α_c and δ_c.

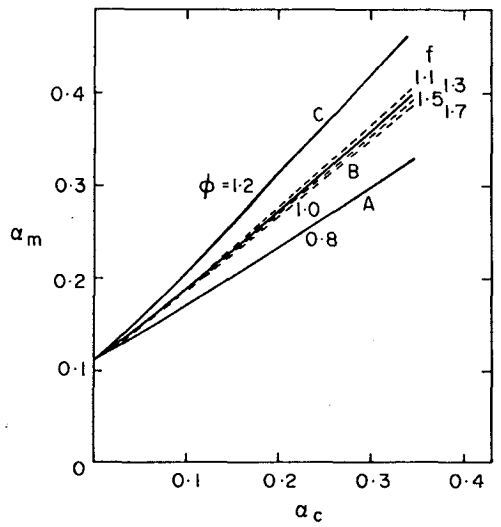

FIG. 11. Effect of varying $\phi(\delta,\theta,\psi)$ and $f(\theta,\delta_c)$ on the relation between α_m and α_c.

A plot of α_m vs α_c for variable values of ϕ and f is shown in Fig. 11. Curves A, B and C correspond to $\phi = 0.8$, 1.0 and 1.2, respectively. When ϕ is varied, f is kept at 1.3; when f is varied, ϕ is kept at 1.0. Now, according to Table 2, f can vary between about 1 and 2, depending on the time and the day. The variation in α_c with f is seen to be minimal, and the quantity $\Delta\alpha_c/\Delta f$ ($\alpha_m = 0.4$, say) $\approx 0.01/0.3 \approx 0.033$. However, the variation in α_c for changes in ϕ is much greater. Thus $(\Delta\alpha_c/\Delta\phi)(\alpha_m \approx 0.3) \approx 0.07/0.215 \approx 0.326$.

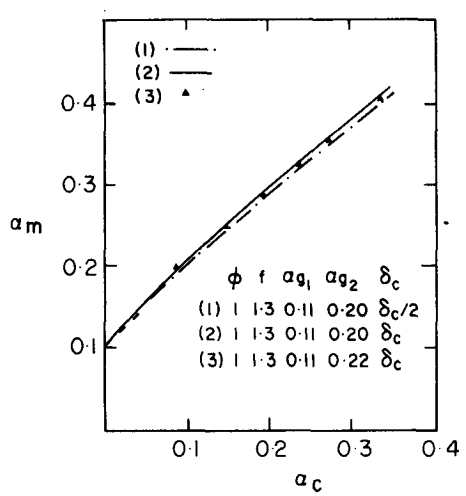

FIG. 12. Effect of varying surface albedo and effective cloud optical depth on the relation between α_m and α_c.

Fig. 12 shows two more effects. First, if α_{g2} (say) is changed by 10% from 0.2 to 0.22, the effect on α_c is almost negligible. Although α_{g2} could contain some reflection from wooded slopes, the albedo over the plains did not appear to vary by more than 10%. Even if the variations in α_{g2} were twice this amount, the error in α_c would only be ~3%. Second, we consider the procedure of writing the effective cloud optical depth δ_c as $\frac{1}{2}\delta_c$, due to near-forward scattering of the diffraction component. If δ_c is used instead of $\frac{1}{2}\delta_c$ in Eq. (11), then curve (2) of Fig. 19 is obtained. This gives about a 5% change in α_c, but the actual change would be less, as at least *some* of the radiation would be forward-scattered.

REFERENCES

Derr, V. E., N. L. Abshire, R. E. Cupp and G. T. McNice, 1976: Depolarization of lidar returns from virga and source cloud. *J. Appl. Meteor.*, **15**, 1200–1203.

Fritz, S., 1954: Scattering of solar energy by clouds of "large drops." *J. Meteor.*, **11**, 291–300.

Hansen, J. E., 1969: Exact and approximate solutions for multiple scattering by cloudy and hazy planetary atmospheres. *J. Atmos. Sci.*, **26**, 478–487.

Jacobowitz, H., 1971: A method for computing the transfer of solar radiation through clouds of hexagonal ice crystals. *J. Quant. Spectros. Radiat. Transfer*, **12**, 691–695.

Liou, K. N., 1973: Transfer of solar irradiance through cirrus cloud layers. *J. Geophys. Res.*, **78**, 1409–1418.

Platt, C. M. R., 1973: Lidar and radiometric observations of cirrus clouds. *J. Atmos. Sci.*, **30**, 1191–1204.

——, 1975: Infrared emissivity of cirrus—simultaneous satellite, lidar and radiometric observations. *Quart. J. Roy. Meteor. Soc.*, **101**, 119–126.

——, 1979: Remote sounding of high clouds, 1: Calculation of visible and infrared optical properties from lidar and radiometer measurements. *J. Appl. Meteor.*, **18**, 1130–1143.

Reynolds, D. W., and T. H. Vonder Haar, 1977: A bi-spectral method for cloud parameter determination. *Mon. Wea. Rev.*, **105**, 447–457.

Shenk, W. E., and R. J. Curran, 1973: A multi-spectral method for estimating cirrus cloud top heights. *J. Appl. Meteor.*, **12**, 1213–1216.

Smith, E. A., and D. L. Loranger, 1977: Radiometric calibration of polar and geosynchronous satellite shortwave detectors for albedo measurements. Presented at the U.S. GATE Summer Workshop, Boulder, Colorado, July.

Stephens, G. L., and Webster, P. J., 1979: Sensitivity of radiative forcing to variable cloud and moisture. *J. Atmos. Sci.*, **36**, 1542–1556.

Wendling, P., 1977: Albedo and reflected radiance of horizontally inhomogeneous clouds. *J. Atmos. Sci.*, **34**, 642–650.